

## EXTRACTING GRAIN BOUNDARIES AND MACROSCOPIC DEFORMATIONS FROM IMAGES ON ATOMIC SCALE \*

BENJAMIN BERKELS <sup>†</sup> ANDREAS RÄTZ <sup>‡</sup> MARTIN RUMPF <sup>§</sup> AXEL VOIGT <sup>¶</sup>

**Abstract.** Nowadays image acquisition in materials science allows the resolution of grains at atomic scale. Grains are material regions with different lattice orientation which are frequently in addition elastically stressed. At the same time, new microscopic simulation tools allow to study the dynamics of such grain structures. Single atoms are resolved experimentally as well as in simulation results on the data microscale, whereas lattice orientation and elastic deformation describe corresponding physical structures mesoscopically. A qualitative study of experimental images and simulation results and the comparison of simulation and experiment requires the robust and reliable extraction of mesoscopic properties from the microscopic image data. Based on a Mumford–Shah type functional, grain boundaries are described as free discontinuity sets at which the orientation parameter for the lattice jumps. The lattice structure itself is encoded in a suitable integrand depending on a local lattice orientation and an elastic displacement. For each grain a lattice orientation and one global elastic displacement function are considered as unknowns implicitly described by the image microstructure. In addition the approach incorporates solid–liquid interfaces. The resulting Mumford–Shah functional is approximated with a level set active contour model following the approach by Chan and Vese. The implementation is based on a finite element discretization in space and a step size controlled, regularized gradient descent algorithm.

**Key words.** image segmentation, elastic lattice deformation, grain boundary extraction, phase field crystal model, transmission electron microscopy

**AMS subject classifications.** 65M60, 68U10, 74E15

**1. Introduction.** This paper deals with the extraction of mesoscopic quantities from microscopic image data in materials science. For many problems on an atomic microscale, it is essential to link the underlying atomic structure to the material properties (electrical, optical, mechanical, etc.). The actual material properties are usually determined on a mesoscopic length scale on which non–equilibrium structures exist, which form and evolve during material processing. For example, local variations of the inter atom distance can be understood as material deformation on the mesoscale and the yield strength of a polycrystal varies with the inverse square of the average grain size. Grains are material regions with different lattice orientation which are typically not in equilibrium. In addition they are frequently observed in an elastically deformed state. Experimental tools such as TEM (transmission electron microscopy) [15] today allow measurements down to an atomic resolution (cf. Fig. 1.1). A reliable extraction of elastic deformations, grains and grain boundaries from these TEM-images is essential for an efficient material characterization. On the other hand, recent numerical simulation tools have been developed for physical models of grain formation and grain dynamics on the atomistic scale. Concerning

---

<sup>†</sup>INSTITUT FÜR NUMERISCHE SIMULATION, UNIVERSITÄT BONN,  
*BENJAMIN.BERKELS@INS.UNI-BONN.DE*

<sup>‡</sup>CRYSTAL GROWTH GROUP, RESEARCH CENTER CAESAR, BONN,  
*RAETZ@CAESAR.DE*

<sup>§</sup>INSTITUT FÜR NUMERISCHE SIMULATION, UNIVERSITÄT BONN,  
*MARTIN.RUMPF@INS.UNI-BONN.DE*

<sup>¶</sup>INSTITUT FÜR WISSENSCHAFTLICHES RECHNEN,  
TECHNISCHE UNIVERSITÄT DRESDEN, *AXEL.VOIGT@TU-DRESDEN.DE*

\*This work was supported by the DFG priority program 1114

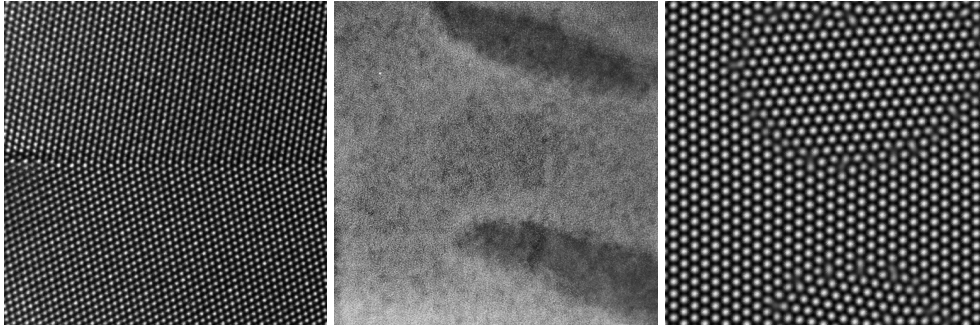


FIG. 1.1. On a TEM image (left), light dots render atoms from a single atom layer of aluminum, in particular this image shows a  $\Sigma 11(113)/[\bar{1}00]$  grain boundary [15] (courtesy of Geoffrey H. Campbell, Lawrence Livermore National Laboratory). On a mesoscale elastic displacements are implicitly encoded in a spatially varying inter atom distance (middle) (courtesy of Nick Schryvers, Antwerpen University). Nowadays, there are physical models like the phase field crystal model which enable numerical simulations of grains. Indeed, a time step from a numerical simulation (right) on the microscale shows a similar atomic layer. In both images, grain boundaries are characterized by jumps in the lattice orientation.

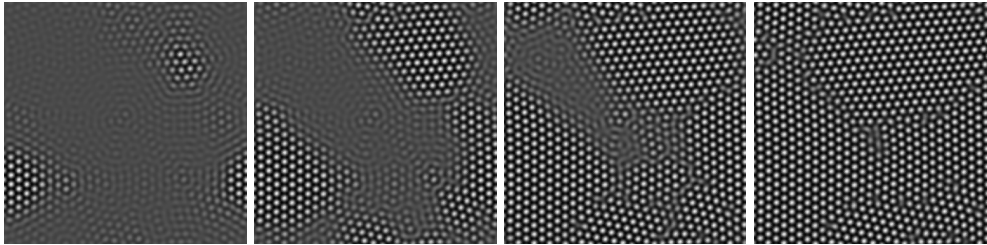


FIG. 1.2. Nucleation of grains in a phase field crystal simulation.

such simulations, we refer to numerical results obtained from a phase field crystal (PFC) model [13] derived from the density function theory (DFT) of freezing [28]. Its methodology describes the evolution of the atomic density of a system according to dissipative dynamics driven by free energy minimization. The resulting highly nonlinear partial differential equation of sixth order can be solved applying a finite element discretization [4]. Such simulations in particular will allow a validation of the physical models based on the comparison of mesoscopic properties such as the propagation speed of grain boundaries. Fig. 1.1 and 1.2 show a comparison of experimental (TEM) and numerically simulated (PFC) single grain boundaries on the atomic scale and the nucleation and growth of grains, respectively.

As mesoscopic material properties result from observations of microstructures their robust and reliable extraction via image processing methodology is expected to provide physical insight in the underlying materials. In this paper we focus on grain segmentation and elastic grain lattice deformation. We aim at a reliable extraction of grain boundaries and in addition of liquid–solid interfaces between the liquid and the solid phase. Thus, we apply a variational approach based on the description of the interfaces by level sets. Furthermore, we generalize the variational approach for the extraction of elastic deformation and a full coupling of orientation and deformation classification. We apply our method to phase field crystal simulation results and

demonstrate the applicability of our approach to experimental images.

Next, let us introduce some basic notation which will be used throughout the paper. We consider a single atom layer resolved on the microscale. In the phase field crystal simulation results as well as in the experimental images, single atoms are represented by blurry, dot-like structures. These dots are either described via the image intensity of the TEM image or the phase field crystal function from the simulation. Let us denote this intensity or phase field crystal by a function  $u : \Omega \subset \mathbb{R}^2 \rightarrow \mathbb{R}$ , where  $\Omega$  is the image domain or the computational domain, respectively. Furthermore, we introduce the lattice orientation as a piecewise constant function  $\alpha : \Omega \subset \mathbb{R}^2 \rightarrow \mathbb{R}$ . We take into account a decomposition of the domain  $\Omega$  into grains, each of them characterized by a constant lattice orientation  $\alpha$ . The grain boundaries form the jump set of the orientation function  $\alpha$ . Furthermore, we assume a global deformation  $\psi : \Omega \rightarrow \mathbb{R}^2$  acting on all grains and reflecting the physical response for instance due to an external loading.

The paper is organized as follows: In Section 2 we review related work. Then, in Section 3 we discuss the case of a single grain with unknown orientation and elastic deformation. The segmentation of grain boundaries in the non deformed case is discussed in Section 4. In both sections we first introduce a variational problem involving sharp interfaces on the microscale describing atomic dot pattern and on the macroscale representing grain boundaries, then discuss a suitable smooth approximation, and derive a minimization algorithm based on a regularized gradient descent. The particular case of a liquid phase beside the solid phase is treated in Paragraph 4.3. Combining the different approaches in Section 5 we derive a joint approach for the simultaneous extraction of grain domains classified by local lattice orientations and the computation of an underlying elastic deformation. Finally, we draw conclusions in Section 6.

**2. Related work.** Our method to be presented here differs to the best of our knowledge significantly from other variational approaches in the literature. Our focus is not on a general purpose texture classification and segmentation tool but on the specific application in materials science. Texture segmentation can be regarded as a two-scale problem, where the microscale is represented by the structure of the texture and the macroscale by the geometric structure of interfaces between differently textured regions. In this sense, we have strong a priori knowledge on the geometric structure of the texture on the microscale and incorporate this directly into the variational approach on the macroscale. Thus, the scale separation is more direct than in other approaches based on a local, direction sensitive frequency analysis. Currently, the post processing of experimental images and the pattern analysis is mostly based on local, discrete Fourier filtering [25].

General image classification has extensively been studied in the last decades. It consists of assigning a label to each point in the image domain and is one of the basic problems in image processing. Classification can be based on geometric and on texture information. Many models have been developed either based on region growing [29, 23, 8], on statistical approaches [6, 7, 18, 19], and in particular recently on variational approaches [3, 2, 10, 20, 31].

The boundaries of the classified regions can be considered as free discontinuity sets of classification parameters, which connects the problem with the Mumford–Shah approach [21] to image segmentation and denoising. A robust and efficient approximation of the Mumford–Shah functional has been presented by Chan and Vese [9] for piecewise constant image segmentation and extended to multiple objects segmenta-

tion based on a multiphase approach [30]. Thereby, the decomposition of the image domain is implicitly described by a single or by multiple level set functions (for a review on level sets we refer to [22, 26]). In [24], their approach has been further generalized for the texture segmentation using a directional sensitive frequency analysis based on Gabor filtering. Texture classification based on the energy represented by selected wavelet coefficients is investigated in [1]. Inspired by the work of Meyer [20] on cartoon and texture decomposition, the classification of geometric and texture information has been investigated further in [3]. There a logic classification framework from [24] has been considered to combine texture classification and geometry segmentation. A combination of level set segmentation and filter response statistics has been considered for texture segmentation in [14]. For a variational texture segmentation approach in image sequences based on level sets we refer to [11].

**3. Macroscopic elastic deformations from deformed lattices.** As already discussed in the introduction, grains are characterized by a homogeneous lattice orientation. At first, let us suppose that there is no liquid phase and we focus on a single grain.

**3.1. Local identification of lattice parameters.** The lattice is uniquely identified by a description of the local neighborhood of a single atom in the lattice. In a reference frame with an atom at the origin, the neighboring atoms are supposed to be placed at positions  $q_i$  for  $i = 1, \dots, m$ , where  $m$  is the number of direct neighbors in the lattice. In case of a hexagonal packing each atom has six direct neighbors at equal distances and we obtain

$$q_i := d \left( \cos \left( i \frac{\pi}{3} \right), \sin \left( i \frac{\pi}{3} \right) \right) \quad i = 1, \dots, 6.$$

Here  $d > 0$  denotes the distance between two atoms. If the lattice from the reference configuration is now rotated by an angle  $\alpha$  and translated to a position  $x$ , the neighboring atoms are located at the positions  $x + M(\alpha)q_i$  where  $M(\alpha)$  is the matrix representation of a rotation by  $\alpha$ , i.e.

$$M(\alpha) := \begin{pmatrix} \cos \alpha & -\sin \alpha \\ \sin \alpha & \cos \alpha \end{pmatrix}.$$

Given an elastic deformation  $\psi$  of the oriented reference lattice we finally observe atoms at positions  $\psi(x + M(\alpha)q_i)$  around a center atom at  $\psi(x)$ .

Let us suppose that  $\theta$  is a suitable threshold for the identification of atom dots described by the function  $u$  and define the indicator function

$$\chi_{[u>\theta]}(x) := \begin{cases} 1; & u(x) > \theta \\ 0; & \text{else} \end{cases}.$$

Then, for a given lattice orientation  $\alpha$ , an elastic deformation  $\psi$  and a point  $x$  with  $\chi_{[u>\theta]}(\psi(x)) = 1$ , we expect  $\chi_{[u>\theta]}(\psi(x + M(\alpha)q_i)) = 1$  as well for  $i = 1, \dots, m$ . Let us suppose that the average radius of a single atom dot is given by  $r$  and define the maximal lattice spacing  $d := \max_{i=1, \dots, m} |q_i|$ . Next, we consider the following identification function  $f$  depending on a lattice orientation  $\alpha$  and on a lattice deformation function  $\psi$ , and evaluated pointwise at positions  $x$ :

$$f[\alpha, \psi](x) = \frac{d^2}{r^2} \chi_{[u>\theta]}(\psi(x)) \Lambda \left( \left( \chi_{[u>\theta]}(\psi(x + M(\alpha)q_i)) \right)_{i=1, \dots, m} \right) \quad (3.1)$$

Here,  $(\chi_i)_{i=1, \dots, m}$  with  $\chi_i := \chi_{[u > \theta]}(\psi(x + M(\alpha)q_i))$  is the vector of displaced and rotated characteristic functions and  $\Lambda : \{0, 1\}^m \rightarrow \mathbb{R}$  a function attaining its global minimum at  $(1, \dots, 1)$  with  $\Lambda(1, \dots, 1) = 0$ . The scaling  $\frac{d^2}{r^2}$  ensures a uniform upper bound of order 1 (in particular independent of  $d$  and  $r$ ) for the integral of  $f$  over the domain of the grain. In what follows we will consider

$$\Lambda(\chi_1, \dots, \chi_m) := \frac{1}{m} \sum_{i=1, \dots, m} (1 - \chi_i).$$

In case the lattice is just rotated and not further deformed, we consider  $\psi$  to be the identical deformation  $\mathbb{1}$  with  $\mathbb{1}(y) = y$  for all  $y$  and simply write  $f[\alpha](x)$ .

One easily verifies that  $f[\alpha, \psi](x) = 0$  if  $x$  is inside a deformed grain with perfect lattice structure, orientation  $\alpha$ , deformed by  $\psi$ , and the distance of  $x$  to the grain boundary in the reference state is at least  $d$ .

**3.2. Lattice deformation and lattice orientation on a single grain.** At first, we consider a bounded domain  $\Omega$  with Lipschitz boundary to represent a single grain and ask for an unknown fixed underlying orientation  $\alpha$  and a deformation  $\psi$ . We phrase this as a minimization problem on the class of constant orientation angles  $\alpha$  and deformations  $\psi$ . Thereby, a fidelity functional measures how well a given  $\alpha$  and  $\psi$  fit to the actually observed lattice structures, whereas a regularity functional acts as a prior on the deformation. The fidelity functional is given by the following integral over the lattice identification function  $f$  depending on both unknowns, the orientation  $\alpha$  and the grain deformation  $\psi$ :

$$E_\Omega[\alpha, \psi] = \int_\Omega f[\alpha, \psi](x) dx \quad (3.2)$$

For  $x$  close to the boundary of the grain  $\Omega$ , this requires the evaluation of  $\psi$  and  $u$  outside  $\Omega$ . Thus, we suppose  $\psi$  to be defined on a sufficiently larger set  $\mathcal{D} \supset \Omega$  with  $\text{dist}(\Omega, \partial\mathcal{D}) \geq d$ . Furthermore, we set  $u(x) = 0$  for  $x \notin \Omega$ . The regularity functional is expected to measure a smoothness modulus of the deformation  $\psi$  on  $\mathcal{D}$ . In the presence of a discontinuous integrand in the deformation - in our case the characteristic function - existence of minimizers can be ensured using a suitable nonlinear elastic regularization energy (for details we refer to [12]). Nevertheless, for the sake of simplicity we confine here to a quadratic energy leading to a linearized elastic regularization in the Euler Lagrange equations. In our model introduced so far, there are effectively two deformations involved. At first, the reference lattice is rotated applying  $M(\alpha)$  and the new configuration is considered as the reference configuration for the physical deformation  $\psi$ . Without any a priori knowledge there is no way to separate a global rotational component in the physical deformation  $\psi$  from the rotation taking care of the proper lattice orientation. But in case of a physically stressed material the axiom of frame indifference applies and we are actually only interested in the non rotational part of the deformation. Thus, taking into account a linearized deformation model we consider the displacement  $\psi - \mathbb{1}$  and the symmetric part of its gradient  $D\psi + D\psi^T - 2\mathbb{1}$  and define the elastic regularization energy

$$E_{\text{elast}}[\psi] = \frac{1}{2} \int_{\mathcal{D}} |D\psi(x) + D\psi(x)^T - 2\mathbb{1}|^2 dx. \quad (3.3)$$

Here, we denote by  $|A| = \sqrt{A : A}$  the Frobenius norm on matrices, where  $A : B = \text{tr}(A^T B)$ . Let us emphasize that we do not impose any specific linear elastic model.

Furthermore, we assume the angular momentum of the deformation of the grain to vanish, i. e.

$$\int_{\Omega} \psi_2(x)x_1 - \psi_1(x)x_2 \, dx = 0. \quad (3.4)$$

This constraint ensures a proper decoupling of a global rotation  $M(\alpha)$  and the linearized elastic deformation  $\psi$  with a vanishing global, linearized rotational component. As an alternative - which turned out to be favorable in case of the numerical implementation - we have taken into account a constraint mean value of the skew symmetric deformation gradient, i. e.  $\int_{\Omega} D\psi(x) - (D\psi)^T(x) \, dx = 0$ , which rules out infinitesimal rotations. Finally, we end up with the energy for the single grain case

$$E_{\text{single}}[\alpha, \psi] = E_{\Omega}[\alpha, \psi] + \mu E_{\text{elast}}[\psi], \quad (3.5)$$

and ask for a minimizer  $(\alpha, \psi)$  of this energy over all admissible lattice rotation angles  $\alpha \in \mathbb{R}$  and all admissible deformations

$$\psi \in \left\{ \tilde{\psi} \in W^{1,2}(\mathcal{D}, \mathbb{R}^2) : \int_{\Omega} \psi_2(x)x_1 - \psi_1(x)x_2 \, dx = 0 \right\}.$$

Here  $W^{1,2}(\mathcal{D}, \mathbb{R}^2)$  denotes the usual space of vector valued functions on  $\mathcal{D}$  with locally square integrable derivatives. Let us remark, that the energy  $E_{\text{elast}}[\psi]$  is translation invariant. Thus, we can expect minimizers only up to a translation which is a multiple of the lattice spacing in each lattice direction. Next, we consider the Euler Lagrange equations for this variational problem. At first, we take into account variations of the fidelity energy. To simplify notation, we rewrite the characteristic function  $\chi_{[u>\theta]}$  of a super level set  $[u > \theta]$  in terms of the heavyside function  $H : \mathbb{R} \rightarrow \mathbb{R}$ , where  $H(t) = 1$  for  $t > 0$  and  $H(t) = 0$  otherwise, and obtain for the indicator function  $f$ :

$$f[\alpha, \psi](x) = \frac{d^2}{mr^2} H(u(\psi(x)) - \theta) \sum_{i=1, \dots, m} (1 - (H(u(\psi(x + M(\alpha)q_i)) - \theta))) .$$

For the variation of the energy with respect to the deformation in a direction  $\zeta$  we get

$$\begin{aligned} \partial_{\psi} E_{\Omega}[\alpha, \psi](\zeta) &= \frac{d^2}{mr^2} \int_{[u \circ \psi = \theta]} \nabla u(\psi(x)) \cdot \zeta(x) \sum_{i=1, \dots, m} (1 - H(u(\psi(x + M(\alpha)q_i)) - \theta)) d\mathcal{H}^1 \\ &\quad - \frac{d^2}{mr^2} \sum_{i=1, \dots, m} \int_{[u \circ \psi = \theta]} H(u(\psi(x - M(\alpha)q_i)) - \theta) \nabla u(\psi(x)) \cdot \zeta(x) d\mathcal{H}^1. \end{aligned}$$

Here, we have applied a shift  $x' = x + M(\alpha)q_i$  for the integration variable in the second row. For the elastic energy we compute

$$\begin{aligned} \partial_{\psi} E_{\text{elast}}[\psi](\zeta) &= \int_{\mathcal{D}} (D\psi(x) + D\psi(x)^T - 2\mathbb{1}) : (D\zeta(x) + D\zeta(x)^T) \, dx \\ &= 2 \int_{\mathcal{D}} (D\psi(x) + D\psi(x)^T - 2\mathbb{1}) : D\zeta(x) \, dx \end{aligned}$$

making use of the symmetry relation  $A^T : B = A : B^T$ . Now, let us consider test functions  $\zeta$  whose support does not intersect the boundary  $[u \circ \psi = \theta]$  of the atomic

dots. Thus, there is no contribution from the variation of the grain energy. Applying integration by parts and the fundamental lemma we end up with the system of partial differential equations  $-2\mu(\Delta\psi + \nabla \operatorname{div} \psi) = 0$  and the corresponding natural boundary condition  $(D\psi^T + D\psi) \cdot \nu = 0$  on  $\partial\mathcal{D}$  in case we do not impose the constraint (3.4). Here  $\nu$  denotes the outer normal on  $\partial\mathcal{D}$ . In the constraint case of vanishing angular momentum (3.4), there appears a Lagrange multiplier  $\lambda$  on the right hand side of the differential equation and we achieve  $-2\mu(\Delta\psi(x) + \nabla \operatorname{div} \psi(x)) = \lambda \begin{pmatrix} 0 & -1 \\ 1 & 0 \end{pmatrix} x$  for  $x \in \mathcal{D} \setminus [u \circ \psi = 0]$ . Next, we consider test functions whose support intersects  $[u \circ \psi = \theta]$  and observe that in this case integration by parts in the elastic energy term leads to the jump term  $2[(D\psi^T + D\psi) \cdot \nu]$ , where  $\nu(x)$  is the normal on  $[u \circ \psi = \theta]$  at position  $x$  and  $[\xi](x) := \lim_{\epsilon \rightarrow 0} \xi(x + \epsilon\nu(x)) - \xi(x - \epsilon\nu(x))$  denotes the jump of a vector valued function on the interface  $[u \circ \psi = \theta]$  at position  $x$ . Thus, we end up with the following jump condition at point  $x$  on  $[u \circ \psi = \theta]$ :

$$\begin{aligned} [(D\psi^T(x) + D\psi(x)) \cdot \nu(x)] &= \frac{d^2}{2m\mu r^2} \nabla u(\psi(x)) \sum_{i=1, \dots, m} \left( H(u \circ \psi(x + M(\alpha)q_i) - \theta) - 1 \right. \\ &\quad \left. + H(u \circ \psi(x - M(\alpha)q_i) - \theta) \right). \end{aligned}$$

The variation with respect to the scalar quantity  $\alpha$  leads to the single scalar equation

$$\begin{aligned} \partial_\alpha E_\Omega[\alpha, \psi] &= -\frac{d^2}{mr^2} \sum_{i=1, \dots, m} \int_{[u \circ \psi = \theta]} H(u \circ \psi(x - M(\alpha)q_i) - \theta) \\ &\quad \nabla u(\psi(x)) \cdot D\psi(x) M'(\alpha) q_i \, d\mathcal{H}^1, \quad (3.6) \end{aligned}$$

where

$$M'(\alpha) = \begin{pmatrix} 0 & -1 \\ 1 & 0 \end{pmatrix} M(\alpha).$$

Finally, the Euler Lagrange conditions to be fulfilled by a minimizer of the functional (3.5) consist of a system of partial differential equations for the deformation  $\psi$  and a single nonlinear equation for the constant orientation value  $\alpha$ , subsumed as follows:

**THEOREM 3.1** (Euler Lagrange conditions in the single grain case). *Suppose the image  $u$  to be smooth and the interface  $[u \circ \psi = \theta]$  to be a set of piecewise smooth curves. Furthermore, assume the minimizing deformation  $\psi$  of (3.5) to be sufficiently smooth as well. Then the following conditions hold for a minimizer  $(\alpha, \psi)$  of the above variational problem: For  $x \in \mathcal{D} \setminus [u \circ \psi = \theta]$  the deformation  $\psi$  solves the system of partial differential equations well-known from linearized elasticity*

$$-2\mu(\Delta\psi(x) + \nabla \operatorname{div} \psi(x)) = \lambda \begin{pmatrix} 0 & -1 \\ 1 & 0 \end{pmatrix} x,$$

with a Lagrange multiplier  $\lambda \in \mathbb{R}$  appearing on the right hand side, on the interface  $[u \circ \psi = \theta]$  the jump condition for the elastic stresses

$$\begin{aligned} [(D\psi^T + D\psi) \cdot \nu] &= \frac{d^2}{2m\mu r^2} (\nabla u) \circ \psi \sum_{i=1, \dots, m} \left( 1 - H(u \circ \psi(\cdot + M(\alpha)q_i) - \theta) \right. \\ &\quad \left. - H(u \circ \psi(\cdot - M(\alpha)q_i) - \theta) \right) \end{aligned}$$

is fulfilled, on  $\partial\mathcal{D}$  the natural boundary condition

$$(D\psi^T + D\psi) \cdot \nu = 0$$

for the outer normal  $\nu$  on  $\partial\mathcal{D}$  holds for the deformation  $\psi$ , and finally  $\alpha$  solves

$$0 = \sum_{i=1, \dots, m} M'(\alpha)q_i \cdot \left( \int_{[u \circ \psi = \theta]} H(u \circ \psi(x - M(\alpha)q_i) - \theta) D\psi(x)^T \nabla u(\psi(x)) \, d\mathcal{H}^1 \right),$$

where  $M'(\alpha) = \begin{pmatrix} 0 & -1 \\ 1 & 0 \end{pmatrix} M(\alpha)$ .

**3.3. Regularization and numerical approximation.** As we have seen above, the discontinuous integrand of the energy  $E_\Omega$  leads to concentration on interfaces bed by level lines in the Euler Lagrange equations. With respect to a robust minimization algorithm and an effective numerical approximation we have to regularize the functionals. Thus, we replace the discontinuous heavyside function  $H$  in the definition of the lattice identification function by a smeared out approximation  $H_\epsilon(s) := \frac{1}{2} + \frac{1}{\pi} \arctan\left(\frac{s}{\epsilon}\right)$  (cf. the regularized Mumford-Shah model by Chan and Vese [9]), where  $\epsilon > 0$ . In fact,  $H'_\epsilon(s) = \frac{\epsilon}{\pi(\epsilon^2 + s^2)}$  converges to  $H'$  in the sense of distributions. We get

$$f_\epsilon[\alpha, \psi](x) = \frac{d^2}{mr^2} H_\epsilon(u(\psi(x)) - \theta) \sum_{i=1, \dots, m} (1 - (H_\epsilon(u(\psi(x + M(\alpha)q_i)) - \theta)))$$

and deduce from that a regularized fidelity energy

$$E_\Omega^\epsilon[\alpha, \psi] = \int_\Omega f_\epsilon[\alpha, \psi](x) \, dx$$

and correspondingly the total regularized energy  $E_{\text{single}}^\epsilon[\alpha, \psi] = E_\Omega^\epsilon[\alpha, \psi] + \mu E_{\text{elast}}[\psi]$ . We choose  $\epsilon = h$ , where  $h$  is the grid size. Thus  $\epsilon$  represents the data resolution on the microscale of the atomic dot pattern. Next, we compute the variation of the energy with respect to a variation  $\zeta$  in the deformation:

$$\begin{aligned} \partial_\psi E_{\text{single}}^\epsilon[\alpha, \psi](\zeta) &= 2\mu \int_{\mathcal{D}} (D\psi(x) + D\psi(x)^T - 2\mathbb{1}) : D\zeta(x) \, dx \\ &\quad + \frac{d^2}{mr^2} \int_\Omega [H'_\epsilon(u(\psi(x)) - \theta) (\nabla u)(\psi(x)) \cdot \zeta(x) \\ &\quad \sum_{i=1, \dots, m} (1 - H_\epsilon(u(\psi(x + M(\alpha)q_i) - \theta)) \\ &\quad - H_\epsilon(u(\psi(x - M(\alpha)q_i) - \theta))] \, dx. \end{aligned}$$

Here, we again have applied the variable transformation  $x' = x + M(\alpha)q_i$  and used the zero extension property of  $u$  outside  $\Omega$ . For the derivative of  $f_\epsilon$  with respect to  $\alpha$  we obtain

$$\begin{aligned} \partial_\alpha f_\epsilon[\alpha, \psi](x) &= -\frac{d^2}{mr^2} \sum_{i=1, \dots, m} (\nabla u(\psi(x + M(\alpha)q_i)) \cdot D\psi(x + M(\alpha)q_i) M'(\alpha)q_i \\ &\quad H_\epsilon(u(\psi(x)) - \theta) H'_\epsilon(u(\psi(x + M(\alpha)q_i) - \theta))). \end{aligned}$$

Finally, straightforward integration of  $\partial_\alpha f_\epsilon$  over  $\Omega$  leads to the variation of the energy with respect to the lattice orientation  $\alpha$ :

$$\partial_\alpha E_{\text{single}}^\epsilon[\alpha, \psi] = \int_\Omega \partial_\alpha f_\epsilon[\alpha, \psi](x) \, dx.$$

A gradient descent algorithm is used for the minimization of the functional  $E_{\text{single}}^\epsilon$ . Each descent step consists of a descent in the deformation  $\psi$ , followed by a corresponding descent in the scalar orientation variable  $\alpha$ . The descent step in the deformation is based on a regularizing metric

$$g(\zeta_1, \zeta_2) = \int_{\mathcal{D}} \zeta_1(x) \cdot \zeta_2(x) + \frac{\sigma^2}{2} D\zeta_1(x) : D\zeta_2(x) \, dx \quad (3.7)$$

on variations  $\zeta_1, \zeta_2$  of the deformation, where  $\sigma$  represents a filter width of the corresponding time discrete and implicit heat equation filter kernel. First we perform a nonconstraint descent in the deformation and then apply a back projection onto the space of deformations with vanishing mean skew symmetric gradient. The gradient descent method looks as follows:

ALGORITHM 3.1 (Gradient descent in the deformation and orientation on a single grain). *Starting from an initial guess  $\psi^0 = \mathbb{1}$  and  $\alpha^0 = 0$  we compute a sequence  $(\alpha^k, \psi^k)_{k=1, \dots}$  such that*

$$\begin{aligned} g(\tilde{\psi}^{k+1} - \psi^k, \zeta) &= -\tau_\psi^k \partial_\psi E_{\text{single}}^\epsilon[\alpha^k, \psi^k](\zeta) \quad \forall \text{variations } \zeta, \\ \psi^{k+1} &= \tilde{\psi}^{k+1} - S(\cdot - x_\Omega), \\ \text{where } S &= \frac{1}{2|\Omega|} \int_\Omega D\tilde{\psi}^{k+1}(x) - (D\tilde{\psi}^{k+1})^T(x) \, dx, \quad x_\Omega = \frac{1}{|\Omega|} \int_\Omega dx, \\ \alpha^{k+1} &= \alpha^k - \tau_\alpha^k \partial_\alpha E_{\text{single}}^\epsilon[\alpha^k, \psi^{k+1}]. \end{aligned}$$

*In both cases Armijo's rule [16] is separately considered as a step size control resulting in different timesteps  $\tau_\psi^k$  and  $\tau_\alpha^k$ .*

Concerning the spatial discretization, we consider bilinear finite elements on the regular grid for the spatial discretization of the deformation  $\psi$ . Each pixel of an experimental image or each node of the regular simulation grid corresponds to a node of the finite element mesh. Furthermore a multiscale minimization strategy is applied. Thus, the algorithm starts with  $\sigma = 1$  and performs the descent until the energy decay per step falls below a given threshold. Then, we decrease  $\sigma$  by a factor  $\frac{1}{2}$  and continue iteratively until a relaxation of the energy is achieved for a filter width  $\sigma$  less than the spatial resolution of a single image pixel. This regularized descent controlled by the scale parameter  $\sigma$  does not affect the energy landscape, but the descent path towards minima. Thus, this type of regularization is conceptually different from the relaxation of the energy itself. Here, the latter is represented by the smoothing of the heavyside function controlled by the parameter  $\epsilon$ . We observed that the regularized descent alone already leads to satisfying results in the applications considered here.

In the applications below, the image resolution ranges from  $129 \times 129$  to  $513 \times 513$  resulting in a corresponding grid size from  $h = 0.0078125$  to  $h = 0.001953125$ . The parameters are chosen as follows:  $d = 0.072552$  (test data),  $r = d$ ,  $\theta \approx 0.5$ ,  $\epsilon = h$ . The coefficient in front of the elastic energy varies from  $\mu = 0.1$  (test data) to  $\mu = 1.0$  (experimental data). In the second row in Figure 3.3 an even stronger elastic energy contribution with  $\mu = 10.0$  turns out to be appropriate. The parameter  $d$  describing

the dot pattern in the experimental images depends on the concrete type of image and is measured based on a small image sample. Figure 3.1 gives an impression about how many grid points are in the transition layer.

We tested the algorithm first on test data for fixed orientation parameter  $\alpha = 0$  and without the constraint on the skew symmetric part of the mean deformation gradient. Thus, the deformation  $\psi$  is expected to recover both a rigid body motion and a non rotational and non translational deformation. Figure 3.2 shows the recovery of different types of deformation for test cases and 3.3 renders the output deformation obtained for experimental data. Furthermore, Figure 3.5 demonstrates the simultaneous detection of  $\alpha$  and  $\psi$  with back projection. Finally, Figure 3.4 depicts the energy decay in a particular application of the descent algorithm. The crosses mark time steps, where the scale parameter  $\sigma$  is refined.

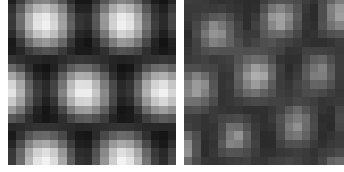


FIG. 3.1. Zoom up of a PFC simulation result (left) and an experimental TEM image (right) showing the resolution of the underlying grid

**4. Segmenting grain boundaries.** In the following section, we will first introduce a Mumford–Shah type model for the segmentation of grain boundaries in the absence of an elastic deformation. Thereby, grains are identified by a homogeneous lattice orientation. In a second step, we will explain how to expand this model in case of an additional solid–liquid interfaces as it appears in particular in case of the phase field crystal simulation of homogeneous nucleation. Later, in Section 5 elastic deformations will be incorporated in the segmentation model and we combine the computation of lattice deformation and orientation and the segmentation of grains in a joint approach.

**4.1. A Mumford Shah type model.** Let us suppose that a domain  $\Omega$  is partitioned into  $n$  open sets  $\Omega_j$  for  $j = 1, \dots, n$ , with  $\Omega_j \cap \Omega_k = \emptyset$  and  $\bigcup_{j=1, \dots, n} \Omega_j = \bar{\Omega}$ . These sets are considered to represent the grains and each  $\Omega_j$  is supposed to be characterized by a spatial homogeneous lattice orientation  $\alpha_j \in \mathbb{R}$ . Furthermore, we suppose that at most three grains meet at a point and that the faces  $\Omega_j \cap \Omega_k$  between two grains  $\Omega_j$  and  $\Omega_k$  are smooth curve segments. We gather the different orientations in a piecewise constant function

$$\alpha = \sum_{j=1, \dots, n} \alpha_j \chi_{\Omega_j}.$$

The grain domains  $\Omega_j$  and the grain orientations  $\alpha_j$  form the set of unknowns. Now, we define a functional  $E_{\text{grain}}$  acting on the set of lattice orientations  $\alpha_j$  and open grain domains  $\Omega_j$  in the spirit of the Mumford–Shah functional:

$$\begin{aligned} E_{\text{MS}}[(\alpha_j, \Omega_j)_{j=1, \dots, n}] &:= \sum_{j=1, \dots, n} (E_{\Omega_j}[\alpha_j, \mathbb{1}] + \eta \text{Per}(\Omega_j)) \\ &= \sum_{j=1, \dots, n} \left( \int_{\Omega_j} f[\alpha_j](x) dx + \eta \text{Per}(\Omega_j) \right). \end{aligned} \quad (4.1)$$

Here,  $\text{Per}(\Sigma)$  denotes the perimeter of a set  $\Sigma$ , i.e. the length of the boundary of the set. The lattice identifier  $f[\alpha_j] := f[\alpha_j, \mathbb{1}]$  plays the role of the segmentation criteria for each grain. A minimizer of this energy is considered as a reliable identification of lattice orientations and corresponding grains. Next, we compute the variation of this

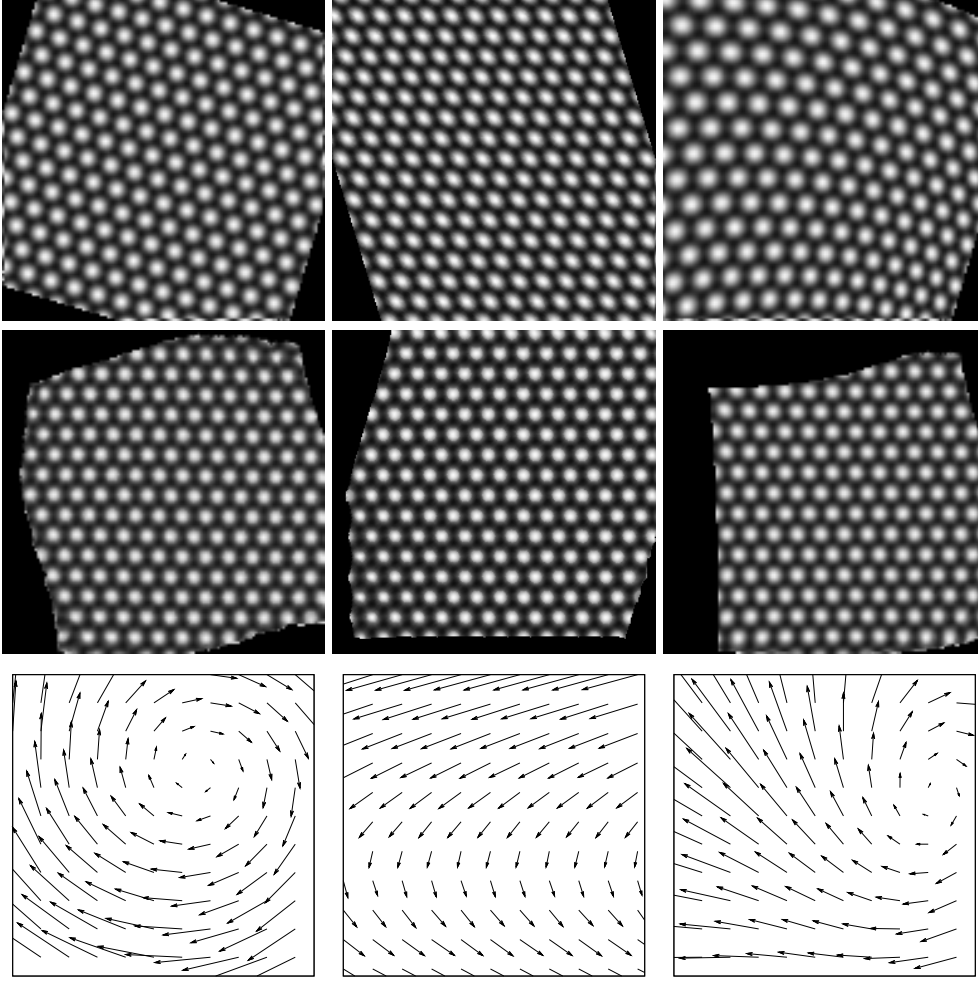


FIG. 3.2. The recovery of a deformation is shown in case of test data representing artificially deformed lattices. The orientation is fixed  $\alpha = 0$  and the constraint on the skew symmetric part of the mean deformation gradient is omitted. The input images  $u$  (top row) reflect different types of deformation: a global rotation, a global shear and a non homogeneous and nonlinear deformation (from left to right). The images  $u \circ \psi$  (middle row) and deformations  $\psi$  (bottom row) are shown.

energy with respect to the shape of the grain domains  $\Omega_j$  and the lattice orientations  $\alpha_j$  for  $j = 1, \dots, n$ . Hence, we consider variations  $\partial\Omega_j + v_j\nu_j$  of the grain boundary in directions of the outward pointing normal  $\nu_j$  for a scalar function  $v_j : \partial\Omega_j \rightarrow \mathbb{R}$ . Based on shape sensitivity analysis [27] we achieve for this normal variation

$$\partial_{\Omega_j} E_{\text{MS}}[(\alpha_k, \Omega_k)_{k=1, \dots, n}](v_j) = \int_{\partial\Omega_j} [f[\cdot]] v_j + \eta \kappa v_j \, d\mathcal{H}^1,$$

where  $[f[\cdot]](x) = f[\alpha_j](x) - f[\alpha_k](x)$  denotes the jump operator applied to  $f$  on a face  $\partial\Omega_j \cap \partial\Omega_k$  between the grain  $\Omega_j$  and an adjacent grain  $\Omega_k$ , and  $\kappa$  the curvature with respect to the normal  $\nu_j$ . Here we assume the variation  $v_j$  to vanish on the

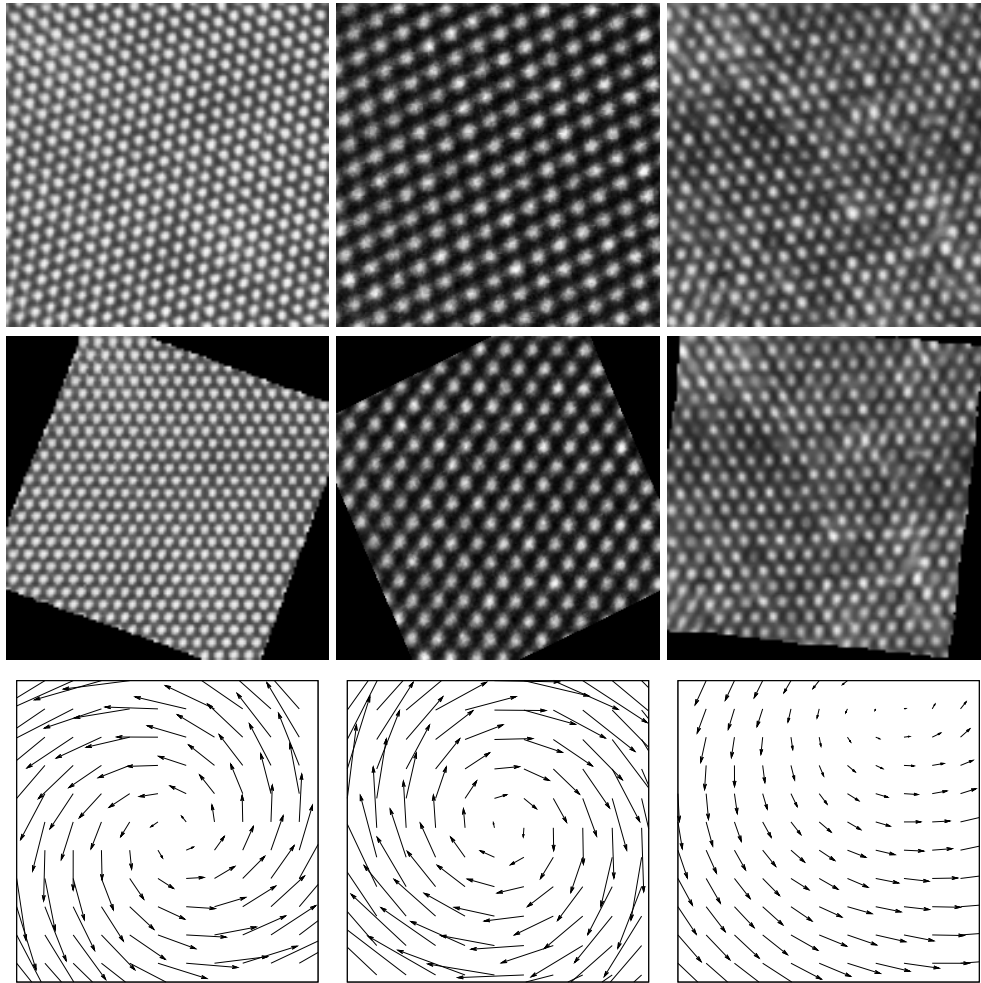


FIG. 3.3. Results are depicted for experimental data (top row) showing single atom layers of different metals / metal alloys: GaN, Al and NiTi. Again the deformation is computed for fixed orientation without a constraint concerning rigid body motions. The pull back  $u \circ \psi^{-1}$  of the images  $u$  into a reference configuration via the computed deformations  $\psi$  are rendered in the middle row, whereas the corresponding deformations  $\psi$  are plotted in the bottom row. The TEM-image in the first column is courtesy of David M. Tricker (Department of Materials Science and Metallurgy, University of Cambridge), the TEM-image in the second column is courtesy of Geoffrey H. Campbell, Lawrence Livermore National Laboratory, the image in the third column is courtesy of Nick Schryvers, Antwerpen University

outer boundary  $\partial\Omega$ . In addition, we observe the usual condition (Young's law) at triple points, i.e. three grains always meet at equal angles of  $\frac{2}{3}\pi$ . The variation of the energy with respect to the lattice orientation  $\alpha_j$  is a straightforward localization

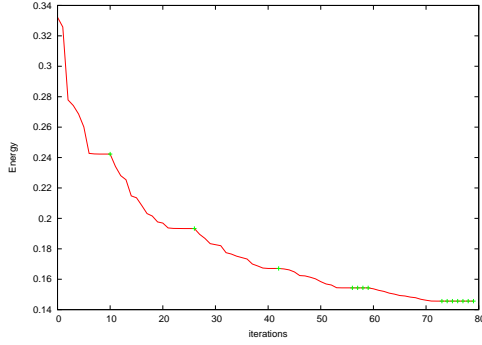


FIG. 3.4. Plot of the energy descent in the relaxation algorithm for the deformation  $\psi$  applied to the data in the first row of figure 3.2. The crosses mark refinements of the scale parameter  $\sigma$ .

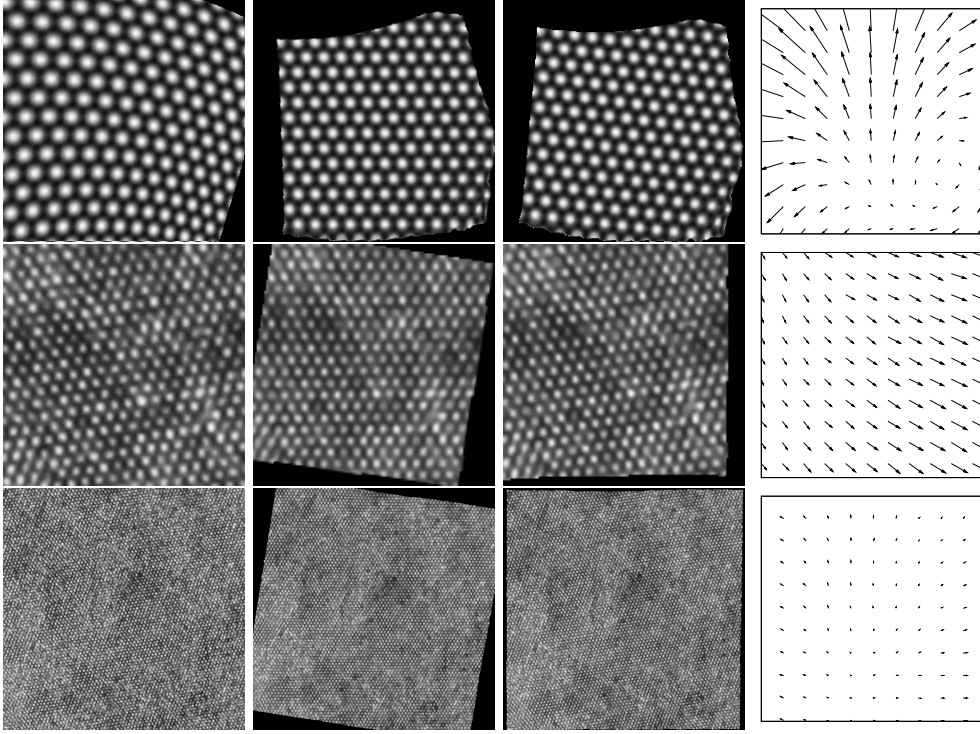


FIG. 3.5. Simultaneous detection of  $\alpha$  and  $\psi$  with back projection: results on an test image deformed by a nonlinear deformation (top) and on experimental images (middle and bottom). From left to right the input image  $u$ , the deformed and rotated image  $u \circ M(-\alpha) \circ \psi^{-1}$ , the deformed image  $u \circ \psi^{-1}$ , and the computed deformation  $\psi$  are depicted. The extracted rotation angles are  $\alpha = 0.119545$  (top row),  $\alpha = -0.152956$  (middle row)  $\alpha = -0.159562$  (bottom row)

of (3.6) and we get

$$\partial_{\alpha_j} E_{\text{MS}}[(\alpha_k, \Omega_k)_{k=1, \dots, n}](v_j) = \frac{d^2}{mr^2} \sum_{i=1}^m \int_{\substack{\Omega_j + M(\alpha_j)q_i \\ \cap [u=\theta]}} H(u(x - M(\alpha_j)q_i) - \theta) \nabla u(x) \cdot M'(\alpha_j)q_i \, d\mathcal{H}^1.$$

Finally, let us summarize the resulting Euler Lagrange conditions for the grain domains  $\Omega_j$  and the grain orientations  $\alpha_j$ :

**THEOREM 4.1** (Euler Lagrange conditions for differently oriented grains). *Suppose the image  $u$  to be smooth and the interface  $[u \circ \psi = \theta]$  to be a set of piecewise smooth curves. Then, a decomposition of  $\Omega$  into grain domains  $\Omega_1, \dots, \Omega_m$  of the above discussed type and a set of grain orientations  $\alpha_1, \dots, \alpha_m$  which minimizes the energy  $E_{MS}$  fulfill the following conditions:*

*On faces  $\bar{\Omega}_j \cap \bar{\Omega}_k$  between grain domains  $\Omega_j$  and  $\Omega_k$*

$$\eta\kappa = -(f[\alpha_j] - f[\alpha_k])$$

*holds for the curvature  $\kappa$  evaluated with respect to the normal pointing outward of the grain  $\Omega_j$ . At triple points the boundary segments of grains meet at angles  $\frac{2}{3}\pi$ . Finally, the orientation  $\alpha_j$  on grain  $\Omega_j$  solves the scalar, nonlinear equation*

$$0 = \sum_{i=1}^m M'(\alpha_j)q_i \cdot \left( \int_{\substack{\Omega_j + M(\alpha_j)q_i \\ \cap [u=\theta]}} H(u(x - M(\alpha_j)q_i) - \theta) \nabla u(x) \, d\mathcal{H}^1 \right).$$

From these conditions we can derive a bound on the curvature  $\kappa$  of the grain boundary segments. In fact, from  $0 \leq f[\alpha] \leq \frac{d^2}{r^2}$  we deduce

$$|\kappa| \leq \frac{d^2}{\eta r^2}$$

and hence for fixed geometric parameters  $d$ ,  $r$  and sufficiently large weight  $\eta$  in front of the shape prior in the energy grain boundary segments tend to straighten.

In case of only two different lattice orientations  $\alpha_1$  and  $\alpha_2$  and corresponding (possibly not connected) domains  $\Omega_1$  and  $\Omega_2$ , we can formulate the variational problem as a problem on the binary function  $\alpha$  and the interface  $\Gamma_G$  between the two sets  $\Omega_1$  and  $\Omega_2$  and obtain (up to the constant term  $\text{Per}(\Omega)$ ) the energy

$$E_{MS}[\alpha_1, \alpha_2, \Gamma_G] := \int_{\Omega_1} f[\alpha_1] \, dx + \int_{\Omega_2} f[\alpha_2] \, dx + 2\eta \mathcal{H}^1(\Gamma_G),$$

where  $\mathcal{H}^1(\cdot)$  denotes the one-dimensional Hausdorff measure.

**4.2. Chan–Vese type regularization and a level set implementation.** To solve the above free discontinuity problems, we again consider a Chan–Vese type approach [9] and rewrite the variational formulation based on an implicit description of the domains via level set functions. We focus here on two different unknown grain orientations  $\alpha_1$  and  $\alpha_2$  and consider a level set function  $\phi$ . Here,  $\phi$  is supposed to define the decomposition into the two grain domains  $\Omega_1$  and  $\Omega_2$ , i. e.  $\Omega_1 = [\phi < 0]$  and  $\Omega_2 = [\phi > 0]$ . Again, making use of the heavyside function, we can rewrite the above Mumford–Shah type energy and obtain

$$E_{CV}[\alpha_1, \alpha_2, \phi] := \int_{\Omega} H(\phi) f[\alpha_2] + (1 - H(\phi)) f[\alpha_1] + 2\nu |\nabla H(\phi)| \, dx \quad (4.2)$$

depending on the level set function  $\phi$  and the two grain orientations  $\alpha_1$  and  $\alpha_2$ . The variational modeling of more than two grain orientations can be based on the

multiple domain segmentation method by Chan and Vese [30] in a straightforward way. In this paper, we confine to the case of only two orientations, but our latest implementation also supports multiphase segmentation (cf. Fig. 4.4). Now, we again take into account a regularized heavyside function  $H_\delta(x) := \frac{1}{2} + \frac{1}{\pi} \arctan\left(\frac{x}{\delta}\right)$  for some  $\delta > 0$  and derive together with the regularization of the indicator function from Section 3.2 a regularized Chan–Vese type energy

$$E_{CV}^{\delta,\epsilon}[\alpha_1, \alpha_2, \phi] := \int_{\Omega} H_\delta(\phi) f_\epsilon[\alpha_2] + (1 - H_\delta(\phi)) f_\epsilon[\alpha_1] + 2\nu |\nabla H_\delta(\phi)| \, dx. \quad (4.3)$$

The desired guidance of the initial zero contour to the actual interfaces to be detected requires a non-local support of the regularized heavyside function. The numerical computation is again based on a gradient descent in the level set function  $\phi$  and two orientation values  $\alpha_1$  and  $\alpha_2$ . Different from the grey value segmentation based on the original approach by Chan and Vese, the energy is not quadratic in the orientation parameters  $\alpha_1$  and  $\alpha_2$  and thus minimization over these two angles is already a non-linear problem. Now, we compute the variation of the energy with respect to the level set function  $\phi$  and the orientations  $\alpha_1$  and  $\alpha_2$ . At first, we consider the regularized perimeter functional  $\text{Per}^\delta[\phi] := \int_{\Omega} |\nabla H_\delta(\phi)| \, dx$ , and obtain

$$\begin{aligned} \partial_\phi \text{Per}^\delta[\phi](\xi) &= \int_{\Omega} \frac{d}{d\epsilon} (H'_\delta(\phi + \epsilon\xi) |\nabla(\phi + \epsilon\xi)|) \Big|_{\epsilon=0} \, dx \\ &= \int_{\Omega} \frac{\nabla\phi}{|\nabla\phi|} \cdot (H''_\delta(\phi) \nabla\phi \xi + H'_\delta(\phi) \nabla\xi) \, dx = \int_{\Omega} \frac{\nabla\phi}{|\nabla\phi|} \cdot \nabla(H'_\delta(\phi)\xi) \, dx. \end{aligned}$$

Thus, for the variation of the energy with respect to the level set function  $\phi$  we get

$$\partial_\phi E_{CV}^{\delta,\epsilon}[\alpha_1, \alpha_2, \phi](\xi) = \int_{\Omega} H'_\delta(\phi) \xi (f_\epsilon[\alpha_2] - f_\epsilon[\alpha_1]) + 2\nu \int_{\Omega} \frac{\nabla\phi}{|\nabla\phi|} \cdot \nabla(H'_\delta(\phi)\xi) \, dx$$

which reflects the sensitivity with respect to modifications of the implicit description of the grain interface  $[\phi = 0]$ . Furthermore, a variation of the energy with respect to one of the grain orientations – we exemplarily pick here  $\alpha_1$  – leads to

$$\partial_{\alpha_1} E_{CV}^{\delta,\epsilon}[\alpha_1, \alpha_2, \phi] = \int_{\Omega} (1 - H_\delta(\phi)) \partial_\alpha f_\epsilon[\alpha_1] \, dx.$$

Now, we again consider a regularized gradient descent in the level set function  $\phi$ . Hence, we use a transformation in the test function, replacing  $H'_\delta(\phi)\xi$  by a new test function again denoted by  $\xi$ . In analogy to (3.7) we define by

$$g(\xi_1, \xi_2) = \int_{\mathcal{D}} \xi_1(x) \xi_2(x) + \frac{\sigma^2}{2} \nabla \xi_1(x) \cdot \nabla \xi_2(x) \, dx \quad (4.4)$$

a metric on scalar variations of the level set function. The resulting algorithm is based on the following iterative descent scheme:

**ALGORITHM 4.1** (Gradient descent for grain segmentation and deformation extraction). *Then, starting from an initial guess of the boundary contour encoded in a level set function  $\phi^0$  and initial values for the two orientation parameters  $\alpha_1^0, \alpha_2^0 = 0$ , we compute a sequence  $(\alpha_1^k, \alpha_2^k, \phi^k)_{k=1, \dots}$  based on successive regularized gradient descent steps in the level set representation*

$$g\left(\frac{\phi^{k+1} - \phi^k}{H'_\delta(\phi)}, \xi\right) = -\tau_\phi^k \int_{\Omega} 2\nu \frac{\nabla\phi^k}{|\nabla\phi^k|} \cdot \nabla\xi + \xi (f_\epsilon[\alpha_2^k] - f_\epsilon[\alpha_1^k]) \, dx \quad \forall \text{variations } \xi$$

for a time step size  $\tau_\phi$  alternated with the corresponding descent step for the two orientation parameters

$$\begin{aligned}\alpha_1^{k+1} &= \alpha_1^k - \tau_\alpha^k \int_{\Omega} (1 - H_\delta(\phi)) \partial_{\alpha_1} f_\epsilon[\alpha_1^k] \, dx \\ \alpha_2^{k+1} &= \alpha_2^k - \tau_\alpha^k \int_{\Omega} H_\delta(\phi) \partial_{\alpha_2} f_\epsilon[\alpha_2^k] \, dx.\end{aligned}$$

A separate Armijo's rule is applied to control each of the two different time steps  $\tau_\phi^k$  and  $\tau_\alpha^k$ .

As in Section 3.3 for the deformation  $\psi$  we now consider bilinear finite elements on the regular grid for the spatial discretization of the level set function  $\phi$ . Regarding numerical methods for levelset propagation by finite elements we refer to [17]. Furthermore, the same type of multi scale minimization strategy is applied for the relaxation of the level set function. For a coarse filter width  $\sigma$  first coarse scale adjustments of  $\phi$  are enforced. Then on successively finer scales more and more of the detailed structure of the grain boundaries can be recovered by the level set function. As pointed out earlier, this regularized descent does not affect the energy landscape, but the descent path towards minima. Even though the level set function  $\phi$  describes grain boundaries on a *mesoscopic scale*, and the lattice identifier functions is given on the *microscale* of the actual atomic dot pattern, the corresponding regularization parameters  $\epsilon$  and  $\delta$  can both be chosen of the order of the grid size. Indeed, we resolve the mesoscopic grain boundaries on the atomic microscale. The achieved accuracy in the spatial position of the grain boundary is of the order of the lattice parameter  $d$ . In case of a smooth grain boundary, we expect a sub-lattice accuracy, due to the symmetric treatment of the lattice indicator function and the overlapping measurement of pattern consistency encoded in this function.

In the applications below, the image resolution ranges from  $129 \times 129$  to  $257 \times 257$  resulting in a corresponding grid size from  $h = 0.0078125$  to  $h = 0.00390625$ . Furthermore, we have chosen the following parameters:  $d = 0.072552$  (test data),  $r = d$ ,  $\theta \approx 0.5$ ,  $\epsilon = \delta = 0.01$ ,  $\eta = 0.05$ . As before, for the experimental images the parameter  $d$  depends on the concrete lattice pattern in the image and is extracted based on a small image sample.

Figure 4.1 shows the energy decay for a specific application of the level set algorithm. The crosses mark time steps, where the scale parameter  $\sigma$  is refined.

At first, we applied the algorithm on test data, generated from homogeneous dots on a lattice with precisely the same lattice spacing as encoded in our algorithm. A simple blending between two such lattices with different orientation is used to generate grain boundary type interfaces. Fig. 4.2 shows the identification of grain boundaries of different amplitude. Furthermore, we applied our method to transmission electron microscopy (TEM) images. The results, shown in Fig. 4.3, in particular demonstrate the robustness of the approach with respect to noise in the experimental data and natural fluctuations in the shape of the atom dots and the lattice spacing. In particular, let us emphasize that the variational method is capable to detect effects on an intermediate scale like the oscillating pattern of the interface in the second picture pair. Finally, in Fig. 4.4 the detection of grain boundaries in a simulation result from a phase field crystal model is demonstrated [4]. Even though we confine to a single levelset function in this paper, our latest implementation also supports segmentation with multiple levelset functions.

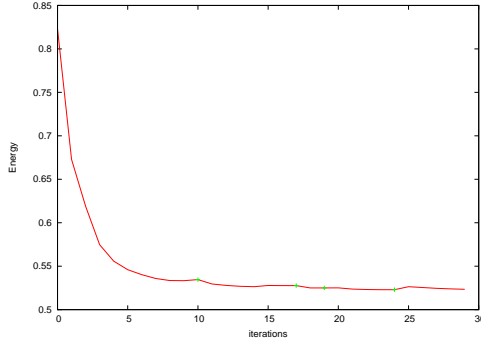


FIG. 4.1. Plot of the energy decay in the level set method for grain boundary extraction applied to the data in the third/forth row of figure 4.3. The crosses mark refinements of the scale parameter  $\sigma$ , which gives rise to a slightly increasing energy in the corresponding step. Redistancing of  $\phi$  is done every five iterations.

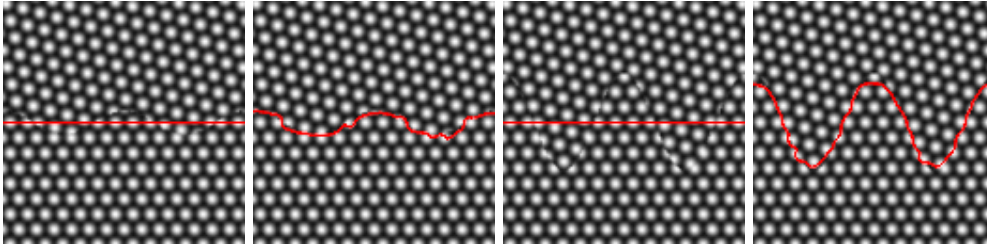


FIG. 4.2. Grain boundary detection on test data: input images  $u$  (first and third picture) with initial zero level set of  $\phi$  and computed grain boundaries (second and fourth picture). Interfaces with different amplitude are considered in the first and second image pair.

**4.3. Simultaneously detecting a liquid–solid interface.** Let us now incorporate the distinction between solid and liquid phase into our variational model. In particular in the simulation results, the solid state is characterized by prominent atom dots with large values of  $u$ . Indeed, taking into account threshold values  $\theta_1$  and  $\theta_2$ , we suppose that  $u(x) > \theta_2$  indicates an atom dot at position  $x$  and vice versa inter-atom regions are characterized by low values of  $u$ , i.e.  $u(x) < \theta_1$ . In the liquid regime there are neither very high nor low values of  $u$ , i.e.  $u(x) \in [\theta_1, \theta_2]$ . Unfortunately, the converse is not true. In transition regions between atom and hole in a solid region  $u$  will attain values between  $\theta_1$  and  $\theta_2$ . But in these transition regions, the gradient of  $u$  exceeds a certain threshold  $\epsilon > 0$ . Thus, we assume  $x$  to be in the liquid phase  $\Omega_L$  if  $u \in [\theta_1, \theta_2]$  and  $|\nabla u| \leq \epsilon$ . A variational description of the domain splitting into a liquid phase  $\Omega_L$  and a solid phase  $\Omega \setminus \Omega_L$  is encoded in the energy

$$E_{\text{phase}}[\Omega_L] = \int_{\Omega_L} q(x) \, dx + \int_{\Omega \setminus \Omega_L} (1 - q(x)) \, dx + \nu \text{Per}(\Omega_L),$$

based on the indicator function

$$\begin{aligned} q(x) &:= 1 - \chi_{[u > \theta_1]}(x) \chi_{[u < \theta_2]}(x) \chi_{[|\nabla u| < \epsilon]}(x) \\ &= \begin{cases} 0 & ; \text{ for } u \in [\theta_1, \theta_2] \wedge |\nabla u| < \epsilon \\ 1 & ; \text{ else. } \end{cases} \end{aligned}$$

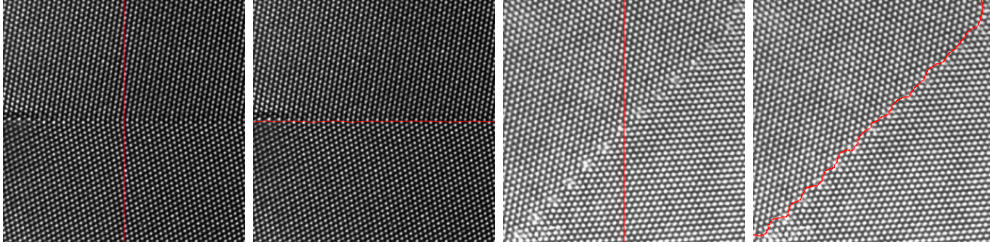


FIG. 4.3. Two results of grain boundary detection on TEM-images: input images  $u$  (first and third picture) with initial position of the zero level set of  $\phi$ , finally detected grain boundaries (second and fourth picture). The TEM-image in the first picture pair is courtesy of Geoffrey H. Campbell, Lawrence Livermore National Laboratory (compare Fig. 1.1), the image used in the second picture pair is courtesy of David M. Tricker (Department of Materials Science and Metallurgy, University of Cambridge) showing a grain boundary in GaN.

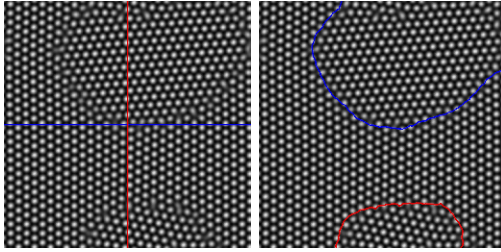


FIG. 4.4. Multiphase grain boundary detection on PFC simulation data: crystal phase field function  $u$  (left) with the initial zero level sets, finally computed grain boundaries (right).

Since  $q = 1$  in the solid region the first term favors to remove solid phase points from  $\Omega_L$ . On the other hand  $q = 0$ , in the liquid region. Hence, it is preferable to remove liquid parts from  $\Omega \setminus \Omega_L$ . In the usual spirit of the Mumford–Shah approach, the third term regularizes the boundary of  $\Omega_L$ .

Now, we merge the two approaches above and simultaneously want to detect the liquid phase  $\Omega_L$  and the solid phase  $\Omega \setminus \Omega_L$  which itself is decomposed into grains  $\Omega_j$ , such that  $\bigcup_j \bar{\Omega}_j = \overline{\Omega \setminus \Omega_L}$ . We end up with the following energy

$$E_{\text{phase,MS}}[\Omega_L, (\alpha_j, \Omega_j)_{j=1, \dots, m}] := \mu \int_{\Omega_L} q(x) \, dx + \mu \int_{\Omega \setminus \Omega_L} (1 - q(x)) \, dx + \nu \text{Per}(\Omega_L) + \sum_{j=1, \dots, n} \left( \int_{\Omega_j} f(x, \alpha_j) \, dx + \eta \text{Per}(\Omega_j) \right). \quad (4.5)$$

The primal decomposition is the one into a liquid and a solid domain. To reflect this in the variational formulation above we consider a relatively large constant  $\mu$ . Indeed, here we choose  $\mu = 10$  and  $\nu = \eta = 0.05$ . Furthermore, we take into account the following values for the other parameters involved:  $\theta = 0.5$ ,  $\theta_1 = 0.3$ ,  $\theta_2 = 0.5$ ,  $\epsilon = 1$  for test data and  $\epsilon = 20$  for phase field crystal simulation data, respectively. For further details on the level set approximation and the concrete numerical relaxation in this special case we refer to [5]. Fig. 4.5 depicts the identification of a liquid–solid interface and a grain boundary on a test data set and for simulation results from a phase field crystal model.

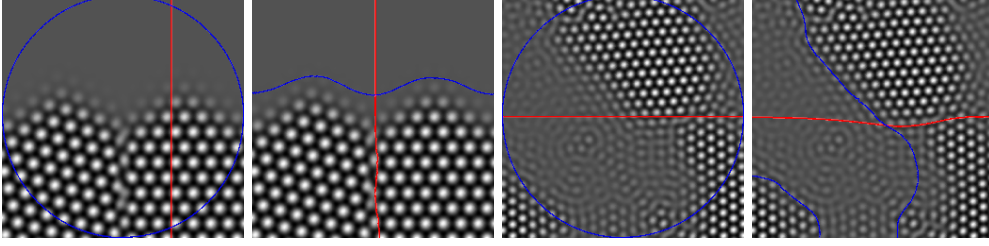


FIG. 4.5. The combined extraction of a liquid–solid interface and a grain boundary is demonstrated. On the left we depict a test input image  $u$  (first picture) with the initial grain boundary level set in red and the initial liquid–solid interface in blue, and the finally computed shape of the grain boundary and the liquid–solid interface location (second picture). On the right the same method is applied to PFC simulation data, showing the crystal phase field function  $u$  (third picture) with the initial positions of the two level sets and the finally extracted liquid–solid and grain boundary interface (fourth picture).

**5. Joint deformation and grain geometry extraction.** Now, we consider a general model, which incorporates grains  $\Omega_j$  of different orientation  $\alpha_j$  and a global elastic deformation  $\psi$  effecting the lattice spacing in the grains. To set up a variational formulation we pick up the energy for the local identification of lattice parameters  $E_{\Omega_j}[\alpha_j, \psi]$  (cf. (3.2)) separately for each grain  $\Omega_j$  and each orientation  $\alpha_j$  and sum them up. Furthermore, we incorporate the perimeter  $\text{Per}(\Omega_j)$  (cf. (4.1)) for all grains and the elastic energy  $E_{\text{elast}}[\psi]$  (cf. (3.3)) for deformations  $\psi$  constraint to vanishing angular momentum. Finally we obtain the following Mumford–Shah type functional for a joint deformation and grain geometry extraction model:

$$E_{\text{joint,MS}}[(\alpha_j, \Omega_j)_{j=1, \dots, n}, \psi] := \sum_{j=1, \dots, n} (E_{\Omega_j}[\alpha_j, \psi] + \eta \text{Per}(\Omega_j)) + \mu E_{\text{elast}}[\psi]$$

For the sake of completeness let us list the variations of this energy with respect to the deformation  $\psi$  in a direction  $\zeta$ , the lattice orientation  $\alpha_j$  on the grain  $\Omega_j$ , and the shape of the grains in the direction of a normal variation  $v_j$ . We achieve

$$\begin{aligned} \partial_{\psi} E_{\text{joint,MS}}[(\alpha_j, \Omega_j)_{j=1, \dots, n}, \psi](\zeta) &= \frac{d^2}{mr^2} \sum_{j=1, \dots, n} \left( \int_{\Omega_j \cap [u \circ \psi = \theta]} \nabla u(\psi(x)) \cdot \zeta(x) \sum_{i=1, \dots, m} (1 - H(u(\psi(x + M(\alpha)q_i)) - \theta)) d\mathcal{H}^1 \right. \\ &\quad \left. - \sum_{i=1, \dots, m} \int_{\substack{\Omega_j + M(\alpha_j)q_i \\ \cap [u \circ \psi = \theta]}} H(u(\psi(x - M(\alpha)q_i)) - \theta) \nabla u(\psi(x)) \cdot \zeta(x) d\mathcal{H}^1 \right) \\ &\quad + 2\mu \int_{\mathcal{D}} (D\psi(x) + D\psi(x)^T - 2\mathbb{1}) : D\zeta(x), \\ \partial_{\alpha_j} E_{\text{joint,MS}}[(\alpha_j, \Omega_j)_{j=1, \dots, n}, \psi] &= \\ &\quad - \frac{d^2}{mr^2} \sum_{i=1}^m \int_{\substack{\Omega_j + M(\alpha_j)q_i \\ \cap [u \circ \psi = \theta]}} H(u \circ \psi(x - M(\alpha_j)q_i) - \theta) \nabla u(\psi(x)) \cdot D\psi(x) M'(\alpha_j) q_i d\mathcal{H}^1, \\ \partial_{\Omega_j} E_{\text{joint,MS}}[(\alpha_k, \Omega_k)_{k=1, \dots, n}, \psi](v_j) &= \int_{\partial\Omega_j} [f[\cdot]] v_j + \eta \kappa v_j d\mathcal{H}^1. \end{aligned}$$

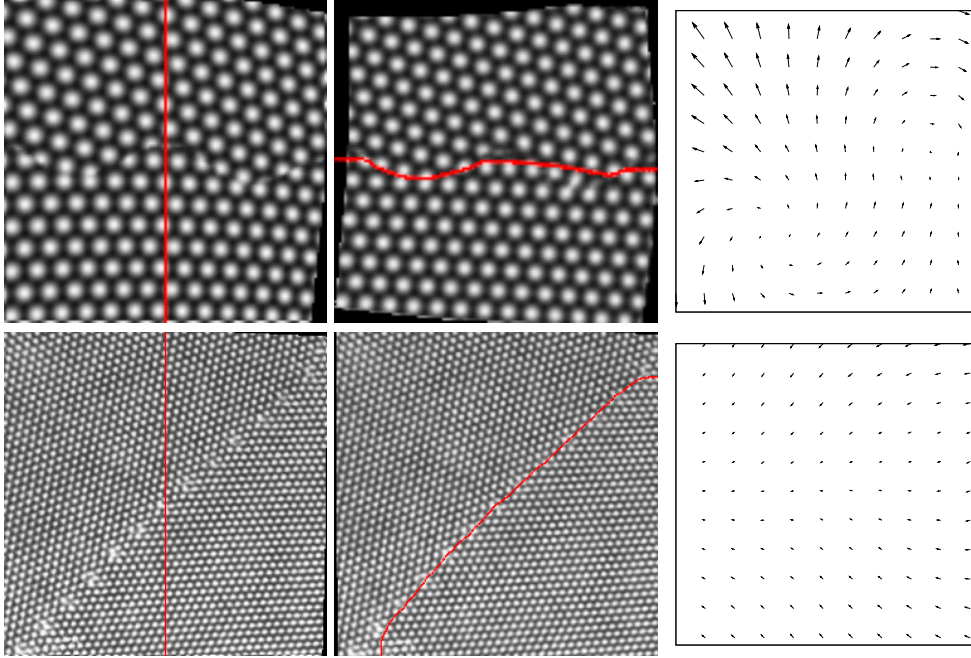


FIG. 5.1. Simultaneous segmentation based on  $\alpha$  and calculation of the deformation  $\psi$ : result on a test image (top) and on a HREM image (bottom) both a posteriori deformed. Initial levelset function (red) on the input image  $u$  (left), computed boundary on the deformed image  $u \circ \psi^{-1}$  (middle) and deformation  $\psi$  found.

With respect to the numerical implementation we again consider a joint Chan–Vese type model for two grains, where the interface between the grains is described by a level set function  $\phi$  as above. Hence, we take into account the energy functional

$$E_{\text{joint,CV}}^{\delta,\epsilon}[\alpha_1, \alpha_2, \phi, \psi] := \int_{\Omega} H_{\delta}(\phi) f_{\epsilon}[\alpha_2, \psi] + (1 - H_{\delta}(\phi)) f_{\epsilon}[\alpha_1, \psi] + 2\nu |\nabla H_{\delta}(\phi)| \\ + \mu \frac{1}{2} \int_{\mathcal{D}} |D\psi(x) + D\psi(x)^T - 2\mathbb{1}|^2 dx.$$

which is to be minimized subject to constraint  $\int_{\Omega} D\psi(x) - (D\psi)^T(x) dx = 0$  on the skew symmetric part of the deformation. The algorithm is a straightforward generalization of the algorithms presented in Section 3.3 and Section 4.2. We implemented an operator splitting, where each iteration consists of a descent step in the deformation  $\psi$  with respect to the metric (3.7), a descent step in the level set function  $\phi$  with respect to the metric (4.4), and two descent steps for the two orientation parameters  $\alpha_1$  and  $\alpha_2$ . As before  $\psi$  and  $\phi$  are discretized using finite elements. Figure 5.1 shows result of the joint approach for a test data set and an a posteriori deformed experimental image.

**6. Conclusions.** We have presented a robust method for the reliable extraction of macroscopic parameters from microscopic images from materials science. The method deals with grains identified by a constant lattice orientation on the corresponding domain and a global elastic deformation acting on these grains and modifying the

local lattice spacing. The local lattice is encoded by an indicator functions for atomic dots describing their spatial relation to adjacent atomic dots. It depends on the local orientation and the deformation. A variational approach is based on an integral over this indicator function and an elastic energy for the deformation acting as a prior. We are able to compute the macroscopic deformation and the lattice orientation on each grain. A Mumford–Shah type variational formulation for the case of multiple grains involves a further prior on the shape of the grains by measuring the perimeter of the grain domains. The numerical implementation is inspired by the segmentation approach by Chan and Vese. The algorithm works equally well on phase field crystal (PFC) simulations and on experimental transmission electron microscopy (TEM) images. It has been extended to detect liquid–solid interfaces. At first, we confine here to the case of two different grain orientations. The straightforward extension to  $2^n$  orientations is currently still work in progress. On still images, the demarcation of such interfaces might be done by hand as well, but will become already very tedious for a large number of grains. For the validation of physical models with experimental data, it is the evolution of the grain boundaries which actually matters. Here, an accurate and robust extraction of interface velocities requires a reliable automatic tool. Thus, an extension of our model to temporal data is envisaged. So far, the lattice orientation is considered as the only local degree of freedom. The type of crystal structure and the atom spacing are preset. In a future generalization one might incorporate further lattice parameters in the variational approach or combine the lattice type classification directly with the variational parameter estimation.

**Acknowledgement.** Benjamin Berkels was supported by the DFG priority program 1114 on time sequence analysis and image processing. Furthermore, we acknowledge Geoffrey H. Campbell for Lawrence Livermore National Lab, Nick Schryvers from Antwerpen University, and David M. Tricker from Cambridge University for generously provided experimental TEM images.

#### REFERENCES

- [1] Jean-François Aujol, Gilles Aubert, and Laure Blanc-Feáaud. Wavelet-based level set evolution for classification of textured images. *IEEE Transactions on Image Processing*, 12(12):1634–1641, 2003.
- [2] Jean-François Aujol and Antonin Chambolle. Dual norms and image decomposition models. *International Journal of Computer Vision*, 63(1):85–104, June 2005.
- [3] Jean-François Aujol and Tony F. Chan. Combining geometrical and textured information to perform image classification. *Journal of Visual Communication and Image Representation*, 17(5):1004–1023, 2006.
- [4] R. Backofen, A. Rätz, and A. Voigt. Nucleation and growth by a phase field crystal (pfc) model. *Phil. Mag. Lett.*, 2007 (accepted).
- [5] B. Berkels, A. Rätz, R. Rumpf, and A. Voigt. Identification of grain boundary contours at atomic scale. In *Proceedings of the First International Conference on Scale Space Methods and Variational Methods in Computer Vision*, pages 765–776. Springer, 2007.
- [6] Marc Berthod, Zoltán Kato, Shan Yu, and Josiane B. Zerubia. Bayesian image classification using markov random fields. *Image and Vision Computing*, 14(4):285–295, May 1996.
- [7] Charles Bouman and Michael Shapiro. Multiscale random field model for bayesian image segmentation. *IEEE Transactions on Image Processing*, 3(2):162–177, March 1994.
- [8] Vicent Caselles, Francine Catté, Tomeu Coll, and François Dibos. A geometric model for active contours in image processing. *Numer. Math.*, 66:1–31, 1993.
- [9] Tony F. Chan and Luminita A. Vese. Active contours without edges. *IEEE Transactions on Image Processing*, 10, no. 2:266 – 277, 2001.
- [10] Daniel Cremers and Christoph Schnörr. Statistical shape knowledge in variational motion segmentation. *Image and Vision Computing*, 21(1):77–86, January 2003.
- [11] G. Doretto, D. Cremers, P. Favaro, and S. Soatto. Dynamic texture segmentation. In B. Triggs

- and A. Zisserman, editors, *IEEE International Conference on Computer Vision (ICCV)*, volume 2, pages 1236–1242, Nice, Oct. 2003.
- [12] M. Droske and M. Rumpf. A variational approach to non-rigid morphological registration. *SIAM Appl. Math.*, 64(2):668–687, 2004.
- [13] K.R. Elder and M. Grant. Modeling elastic and plastic deformations in nonequilibrium processing using phase field crystals. *Physical Review E - Statistical, Nonlinear, and Soft Matter Physics*, 70(5 1):051605–1–051605–18, November 2004.
- [14] Matthias Heiler and Christoph Schnörr. Natural image statistics for natural image segmentation. *IJCV*, 63(1):5–19, 2005.
- [15] Wayne E. King, Geoffrey H. Campbell, Stephen M. Foiles, Dov Cohen, and Kenneth M. Hanson. Quantitative HREM observation of the  $\Sigma 11(113)/[\bar{1}00]$  grain-boundary structure in aluminium and comparison with atomistic simulation. *Journal of Microscopy*, 190(1-2):131–143, 1998.
- [16] P. Kosmol. *Optimierung und Approximation*. de Gruyter Lehrbuch, 1991.
- [17] Omar Lakkis and Ricardo H. Nochetto. A posteriori error analysis for the mean curvature flow of graphs. *SIAM J. Numer. Anal.*, 42(5):1875–1898, 2004.
- [18] Sridhar Lakshmanan and Haluk Derin. Simultaneous parameter estimation and segmentation of gibbs random fields using simulated annealing. *IEEE Transactions on Pattern Analysis and Machine Intelligence*, 11(8):799–813, 1989.
- [19] B. S. Manjunath and Rama Chellappa. Unsupervised texture segmentation using markov random field models. *IEEE Trans. Pattern Anal. Mach. Intell.*, 13(5):478–482, 1991.
- [20] Yves Meyer. *Oscillating Patterns in Image Processing and Nonlinear Evolution Equations: The Fifteenth Dean Jacqueline B. Lewis Memorial Lectures*. American Mathematical Society, Boston, MA, USA, 2001.
- [21] D. Mumford and J. Shah. Optimal approximation by piecewise smooth functions and associated variational problems. *Communications on Pure Applied Mathematics*, 42:577–685, 1989.
- [22] S. J. Osher and R. P. Fedkiw. *Level Set Methods and Dynamic Implicit Surfaces*. Springer-Verlag, 2002.
- [23] Nikos Paragios and Rachid Deriche. Geodesic active regions and level set methods for motion estimation and tracking. *Comput. Vis. Image Underst.*, 97(3):259–282, 2005.
- [24] Berta Sandberg, Tony Chan, and Luminita Vese. A level-set and gabor-based active contour algorithm for segmenting textured images. Technical Report 02-39, UCLA CAM Reports, 2002.
- [25] D. Schryvers et al. Measuring strain fields and concentration gradients around  $\text{Ni}_4\text{Ti}_3$  precipitates. *Materials science and engineering A: structural materials properties microstructure and processing. Special Issue*, 438:485–488, 2006.
- [26] J.A. Sethian. *Level Set Methods and Fast Marching Methods*. Cambridge University Press, 1999.
- [27] J. Sokolowski and J.-P. Zolésio. *Shape sensitivity analysis*, chapter Introduction to shape optimization. Springer, 1992.
- [28] Y. Singh. Density-functional theory of freezing and properties of the ordered phase. *Physics Reports*, 207(6):351–444, 1991.
- [29] Michael Unser. Texture classification and segmentation using wavelet frames. *IEEE Transactions on Image Processing*, 4(11):1549–1560, November 1995.
- [30] Luminita Vese and Tony F. Chan. A multiphase level set framework for image segmentation using the mumford and shah model. *International Journal of Computer Vision*, 50(3):271–293, December 2002.
- [31] Luminita Vese and Stanley Osher. Modeling textures with total variation minimization and oscillating patterns in image processing. *Journal of Scientific Computing*, 19(1-3):553–572, December 2003.